Global Biogeochemical Cycles

Supporting Information for

Processes driving global interior ocean pH distribution

Lauvset, S.K.*[1], Carter, B.R.[2,3], Perez, Fiz F.[4], Jiang, L.-Q.[5,6], Feely, R.A.[3], Velo, A.[4], Olsen, A.[7]

[1]NORCE Norwegian Research Centre, Bjerknes Centre for Climate Research, Bergen, Norway

[2]Joint Institute for the Study of the Atmosphere and Ocean, University of Washington, Seattle, Washington, USA.

[3]Pacific Marine Environmental Laboratory, National Oceanic and Atmospheric Administration, Seattle, Washington, USA.

[4]Instituto de Investigaciones Marinas, IIM– CSIC, Vigo, Spain.

[5]Earth System Science Interdisciplinary Center, University of Maryland, College Park, Maryland, USA.

[6]National Centers for Environmental Information, National Oceanographic and Atmospheric Administration, 1315 East West Hwy, Silver Spring, Maryland, 20910.

[7]Geophysical Institute, University of Bergen and Bjerknes Centre for Climate Research, Bergen, Norway

*Corresponding author: siv.lauvset@norceresearch.no, previously also at Geophysical Institute, University of Bergen

Contents of this file

Text S1 to S6
Figures S1 to S16

Supplementary Text S1 - Water mass ages

Since we here use anthropogenic carbon estimates based on the TTD method we also present water mass ages based on CFC-12 (Figure S1). We are aware that CFC-12 underestimates water mass age in the deepest and oldest water, but the spatial pattern is nevertheless robust. For comparison, we also looked at the GLODAPv1 database [*Key et al.*, 2004], which includes data of the water mass age based on radiocarbon (^{14}C). The correlation identified between remineralized carbon and water mass age (section 3.1) is rather better when the conventional radiocarbon age is used. Below 500 m the correlation between radiocarbon age and remineralized carbon is 0.68 (n=11546) and below 1000 m it is 0.84 (n=8453) with a rate of increase of DIC of 0.10±0.1 µmol kg^{-1} yr^{-1}.

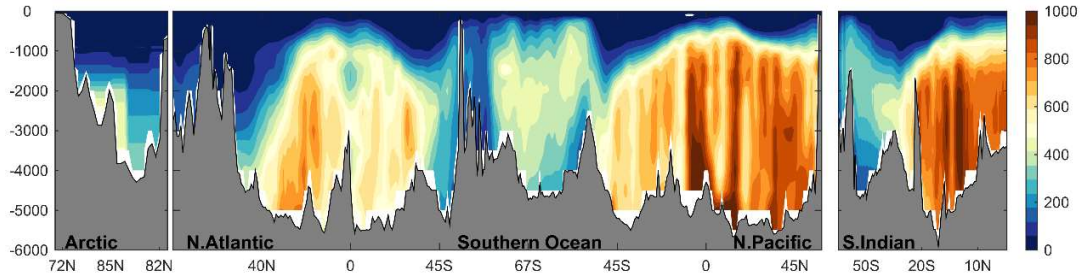

Figure S1. Vertical cross-sections, along the transects shown in Figure 1, showing the water mass age (year) derived from CFC-12 and the transit time distribution (TTD) method. The vertical axis shows depth (m) below sea level.

Supplementary Text S2 - The impact of temperature on pHAn operational aspect related to temperature comes from the methodological practice of referencing and measuring pH at a constant temperature (usually 25 °C). The effect of referring the pH in the water column at 25 ºC instead of the *in situ* temperature is quantified as:

$$\Delta pH^{T} = pH^{f(DIC,TA)}_{T=25℃} - pH^{f(DIC,TA)} \qquad \text{Eqn. S1}$$

Warming decreases pH so normalizing pH to 25 °C, which is almost always warmer than the *in situ* temperature, acts to decrease pH (Figure S2). On the surface (Figure S2a) the spatial variability is large since the temperature gradients are large, and in the equatorial region and the subtropical gyres where surface temperatures can exceed 25 °C $pH^{f(DIC,TA)}_{T=25℃}$ is slightly higher than pH^{2002}. Since interior ocean temperatures are relatively homogeneous (because most water mass formation happens at high latitudes), there is

almost no spatial variability in the impact of temperature in the interior ocean (Figure S2b). Along our section ΔpH^T is typically 0.32±0.05 below 1500 m.

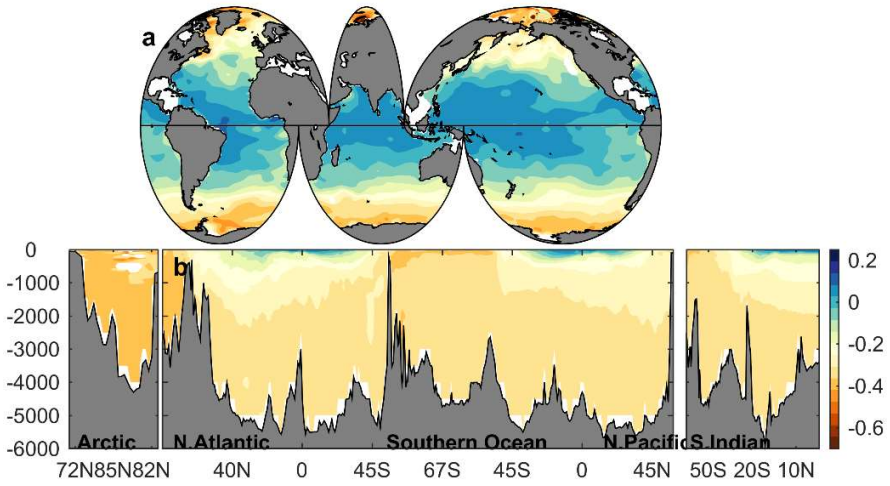

Figure S2. ΔpH^T (Eqn. S1) a) on the surface (20 m) and b) along the transect shown in Figure 1. The color scale is the same for both subplots and matches that in Figure 5. The vertical axis shows depth (m) below sea level.

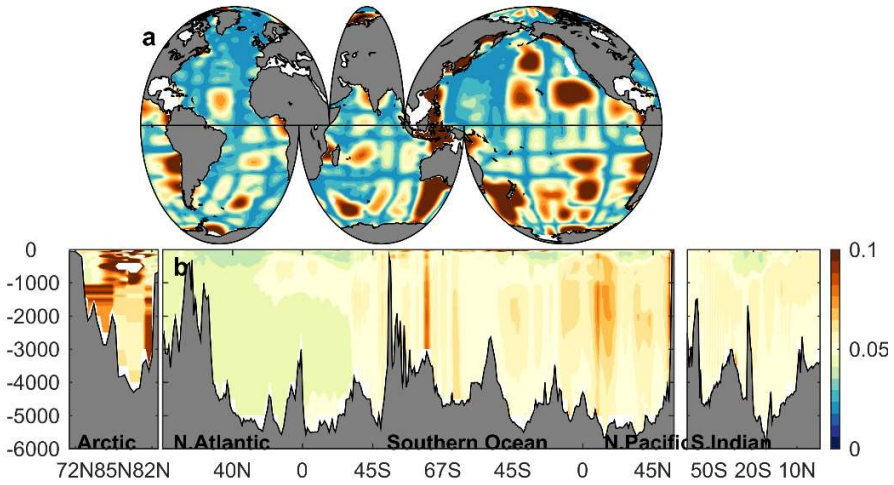

Figure S3. Uncertainties associated with ΔpH^T as shown in Figure S2. The vertical axis shows depth (m) below sea level.

Supplementary Text S3 - Uncertainties

Uncertainties in the estimated changes in DIC and TA due to organic matter remineralization are propagated using the standard uncertainties for input variables given in Table 1 and standard first-order Taylor series expansion (Eqns. S2-S3). For all other calculated variables the uncertainties are given as combined uncertainties summed in

quadrature (Eqns. S4-S15). All pH variables ($\sigma_{pH...}$ as indicated in Eqns. S11-S15) are calculated in CO2SYS for Matlab®, and the uncertainties are calculated using the associated errors.m routine [*Orr et al.*, 2018]. The choice of constants is as described in section 2.3.

$$\sigma_{DIC_{org}} = DIC^{org}\sqrt{\left(\frac{\sigma_{rCO}}{rCO}\right)^2 + \left(\frac{\sigma_{AOU}}{AOU}\right)^2} \quad \text{Eqn. S2}$$

$$\sigma_{TA_{org}} = TA^{org}\sqrt{\left(\frac{\sigma_{1.36}}{1.36}\right)^2 + \left(\frac{\sigma_{rNO}}{rNO}\right)^2 + \left(\frac{\sigma_{AOU}}{AOU}\right)^2} \quad \text{Eqn. S3}$$

$$\sigma_{TA_{CaCO3}} = \sqrt{\sigma_{TA}^2 + \sigma_{TA0}^2 + \sigma_{TA_{org}}^2} \quad \text{Eqn. S4}$$

$$\sigma_{DIC0} = \sqrt{\sigma_{DIC}^2 + \sigma_{Canth}^2 + \sigma_{DIC_{org}}^2 + \sigma_{TA_{CaCO3}}^2} \quad \text{Eqn. S5}$$

$$\sigma_{DIC-Canth} = \sqrt{\sigma_{DIC}^2 + \sigma_{Canth}^2} \quad \text{Eqn. S6}$$

$$\sigma_{DIC-D\ \ CaCO3} = \sqrt{\sigma_{DIC}^2 + (\frac{1}{2}\sigma)_{TA_{CaCO3}}^2} \quad \text{Eqn. S7}$$

$$\sigma_{TA-T\ \ CaCO3} = \sqrt{\sigma_{TA}^2 + \sigma_{TA_{CaCO}}^2} \quad \text{Eqn. S8}$$

$$\sigma_{DIC-DIC_{CaCO3}-DIC_{org}} = \sqrt{\sigma_{DIC}^2 + \sigma_{DIC_{org}}^2 + (\frac{1}{2}\sigma)_{TA_{CaCO3}}^2} \quad \text{Eqn. S9}$$

$$\sigma_{TA-TA_{CaCO3}-TA_{org}} = \sqrt{\sigma_{TA}^2 + \sigma_{TA_{org}}^2 + \sigma_{TA_{CaCO3}}^2} \quad \text{Eqn. S10}$$

$$\sigma_{\Delta pH_{anth}} = \sqrt{\sigma_{pH_{DIC,TA}}^2 + \sigma_{pH_{DIC-Canth,TA}}^2} \quad \text{Eqn. S11}$$

$$\sigma_{\Delta pH_{CaCO3}} = \sqrt{\sigma_{pH_{DIC,TA}}^2 + \sigma_{pH_{DIC-DIC_{CaCO3},TA-TA_{CaCO3}}}^2} \quad \text{Eqn. S12}$$

$$\sigma_{\Delta pH_{org}} = \sqrt{\sigma_{pH_{DIC-DIC_{CaCO3},TA-TA_{CaCO3}}}^2 + \sigma_{pH_{DIC-DIC_{CaCO3}-DICorg,TA-TA_{CaCO3}-TA_{org}}}^2} \quad \text{Eqn. S13}$$

$$\sigma_{\Delta pH^{press}} = \sqrt{\sigma_{pH_{DIC,TA}}^2 + \sigma_{pH_{P=0}}^2} \quad \text{Eqn. S14}$$

$$\sigma_{\Delta pH^{T}} = \sqrt{\sigma_{pH_{DIC,TA}}^2 + \sigma_{pH_{T=25°C}}^2} \quad \text{Eqn. S15}$$

For many parameters calculated in this study the uncertainty is dominated by the mapping error, which to a large degree depends on data density [see *Lauvset et al.*, 2016 for details], and is therefore largest in areas where we have little data (*e.g.*, the Arctic Ocean).

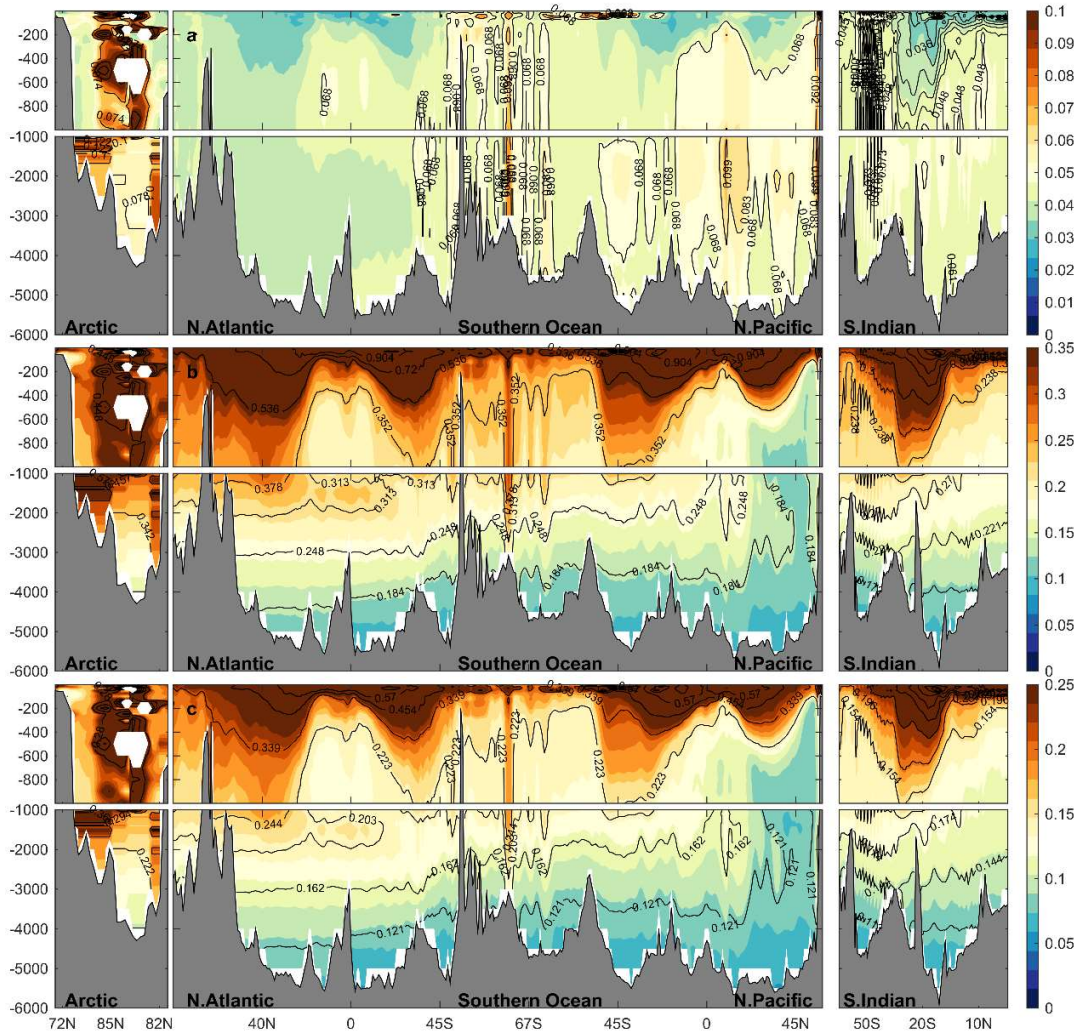

Figure S4. Uncertainties associated with the crossections presented in Figure 2. Note that the three different panels have different color scales. The vertical axis shows depth (m) below sea level.

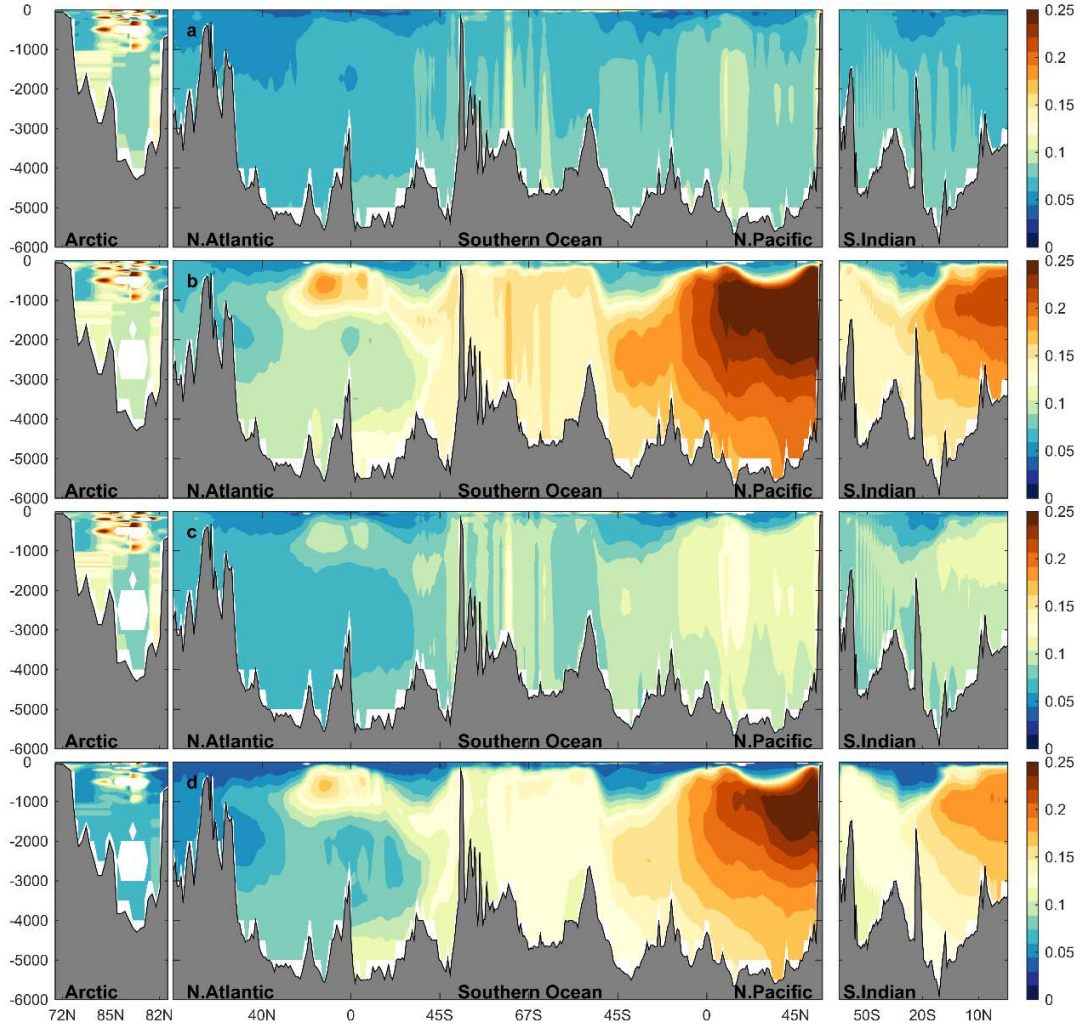

Figure S5. Uncertainties in the crossections presented in Figure 3. The vertical axis shows depth (m) below sea level.

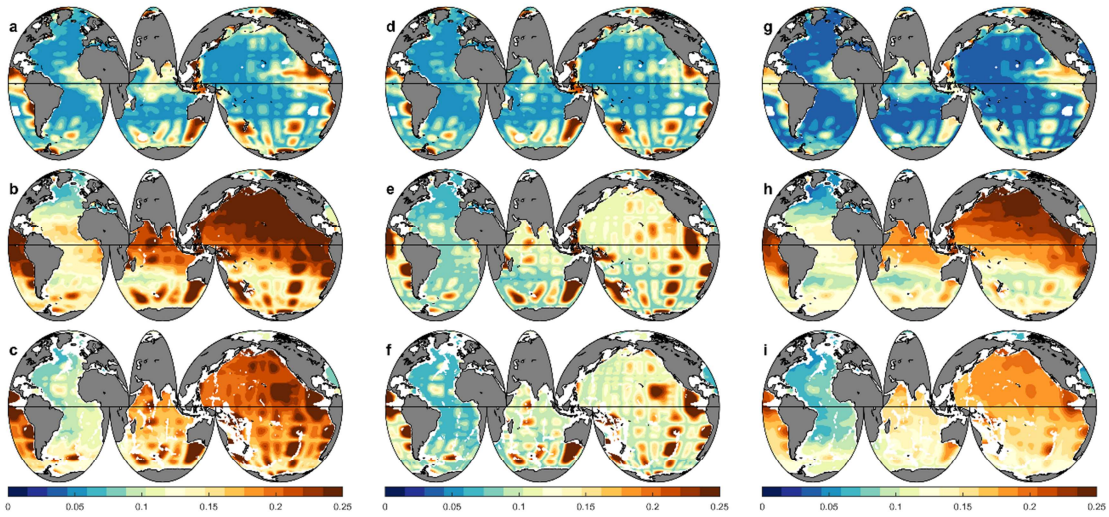

Figure S6. Uncertainties associated with the results presented in Figure 4.

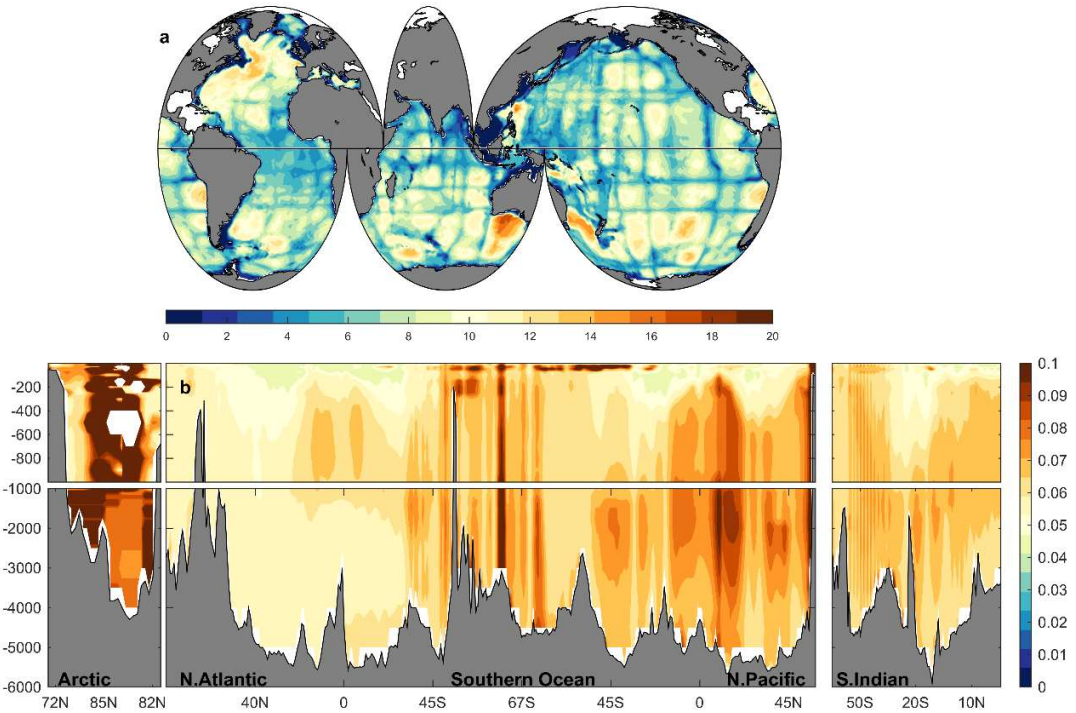

Figure S7. Uncertainties associated with Figure 5. The vertical axis shows depth (m) below sea level.

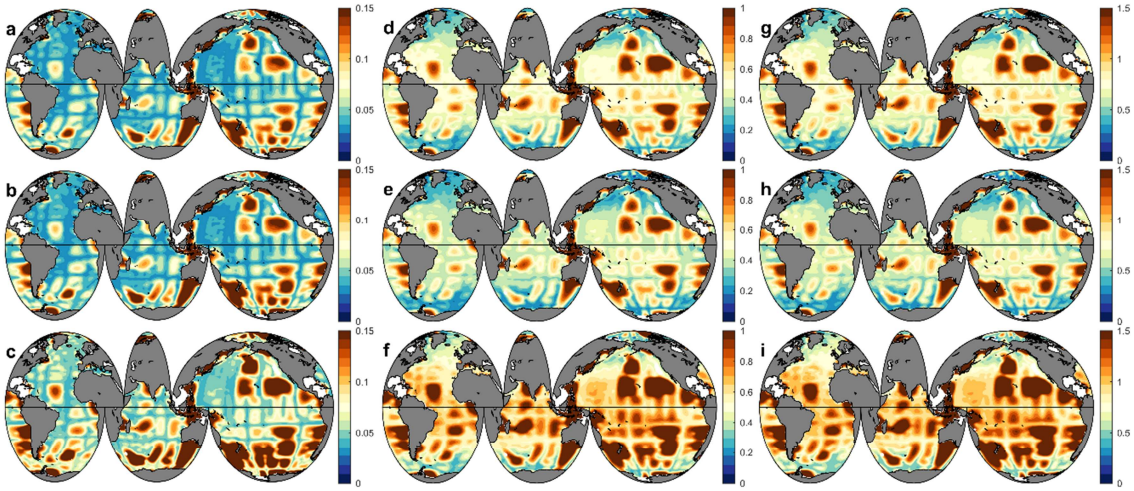

Figure S8. Uncertainties associated with the results presented in Figure 6.

We have in this work quantified the uncertainties in all our calculated values using a formal uncertainty propagation method. While this method is correct, and we have used appropriate estimates for the uncertainty in all input variables and parameters (Table 1), there are some caveats worth mentioning. One is the assumption of uncorrelated uncertainties in DIC and TA detailed in section 2.5. Another is that the results we present here (except those in Figures 2 and 5a) are all differences. As such, the systematic component of the uncertainties in variables and parameters used in calculating pH (and Ω) should cancel. Thus, the slightly smaller $\sigma(pK_1)$ and $\sigma(pK_1)$ of 0.0055 and 0.01 respectively should have been used rather than the values given in Table 1. In addition, *Orr et al.* [2018] argue that when considering the change from one time period to another all uncertainty in the thermodynamic constants can be assumed to cancel out as long as we assume no change in temperature or salinity. The same argument holds for our differences (Eqns. 2-4), thus we could have neglected to include uncertainties from the thermodynamic constants in our estimates. Since we have not the uncertainties we present here are overestimated. In the case of anthropogenic changes in surface ocean pH and Ω (as detailed in section 3.2) removing all uncertainty due to the constants reduce the global average uncertainty to ±0.05, ±0.55, and ±0.86 for ΔpH^{anth}, $\Delta\Omega_{Ar}{}^{anth}$, and $\Delta\Omega_{Ca}{}^{anth}$ respectively. We have made no attempt to separate the uncertainties in DIC and TA, or those from Eqns. S1-S10, into systematic and random components, and therefore

propagate these as random uncertainties. If there is a systematic component to the uncertainties in these then that will also cancel in the differences and further reduce the overall uncertainty estimates for Eqns. 2-6.

The presented uncertainty for the globally averaged surface ocean anthropogenic change in pH and Ω (section 3.2) is very large. In addition to the overestimation due to including uncertainties from the constants a significant component of the overall uncertainty is due to the mapping error on the GLODAPv2 climatological fields we use in this study. If we average only over those cells where there are observations present the global average ΔpH^{anth} is -0.10±0.06. If we further cancel out all uncertainties in the constants the result is -0.10±0.03. Note that the mapping error used here is very large in locations where there are no data and that it increases with distance from the observations [*Lauvset et al.*, 2016]. For the surface estimates this greatly influence the overall uncertainty (due to low data density), but for the cross-sections presented in this study the impact of the mapping uncertainty is very small since the data density is high along these sections. Thus, uncertainties along the cross-sections will not reduce if the mapping error component is removed. The fact that the anthropogenic changes presented in this study have large uncertainties should not be interpreted as these changes being insignificant. We know from the carbonate chemistry that the increased CO_2 concentration has resulted in increased surface ocean acidity. That it is proving difficult to quantify the magnitude of this change globally is a factor of the current inadequacies in our understanding of the thermodynamics of the carbonate chemistry, which leads to non-negligible uncertainties in the constants, as well as the very low data density in GLODAPv2.

Supplementary Text S4 - DIC^{org} and the rate of remineralization

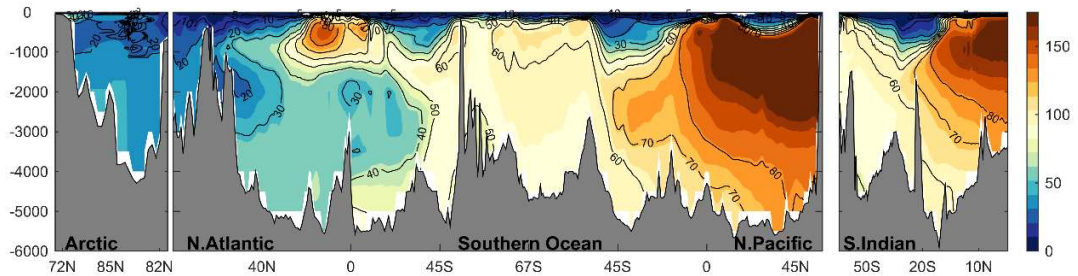

Figure S9. Vertical cross-sections, along the transects shown in Figure 1, showing DIC^{org} (Eqn. 7, µmol C kg^{-1}). The contours indicate uncertainties. Regions where the mapping errors are unacceptable [*Lauvset et al., 2016*] are white. The vertical axis shows depth (m) below sea level.

The spatial distribution of DIC^{org} (Figure S9) completely dominates the spatial pattern of ΔpH^{org} (Figure 3b), as does its uncertainty (Figure S5b). The $pH^{PI,0}{}_{P=0}$ calculated using AOU to determine remineralization effects has the expected uniform distribution of $pH^{PI,0}{}_{P=0}$ in the ocean (Figure 3d). We also see that the interior ocean $pH^{PI,0}{}_{P=0}$ (Figure 3d and 5a) is comparable to the 20 m $pH^{PI,0}{}_{P=0}$ in known water mass formation areas (Figure 4g). The estimation using AOU produces $pH^{PI,0}{}_{P=0}$ values (8.20±0.13) very similar to those expected considering a pre-industrial molar fraction 280 ppm (8.18±0.01).
To visualize the rate of remineralization we calculate an analogue to the oxygen utilization rate by dividing ΔpH^{org} by water mass age (Figure S10-S11).

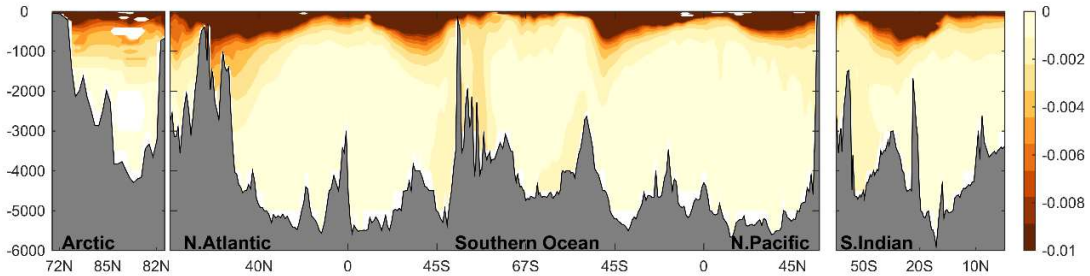

Figure S10. Vertical cross-section (along transects shown in Figure 1) showing the rate of remineralization, defined as $\frac{\Delta pH^{org}}{\Gamma}$, where Γ is the water mass age defined by the TTD (Section 2.3). The vertical axis shows depth (m) below sea level.

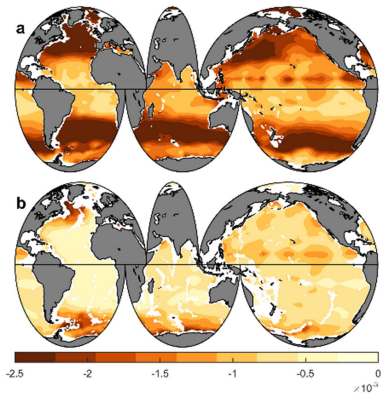

Figure S11. Maps showing the rate of remineralization, defined as in Figure S10, at 20 m, 1000 m, and 3000 m. Note that in order to highlight features in the deep ocean the color scale is not the same as in Figure S10.

Supplementary Text S5 - Preformed properties

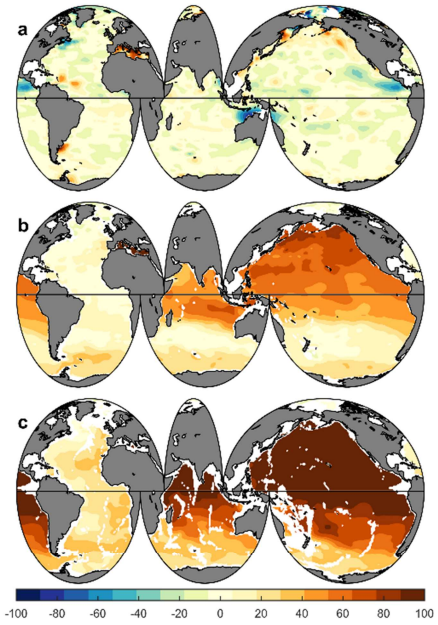

Figure S12. Maps showing TA (GLODAPv2) minus TA^0 (TMI) at surface, 1000m and 3000m.

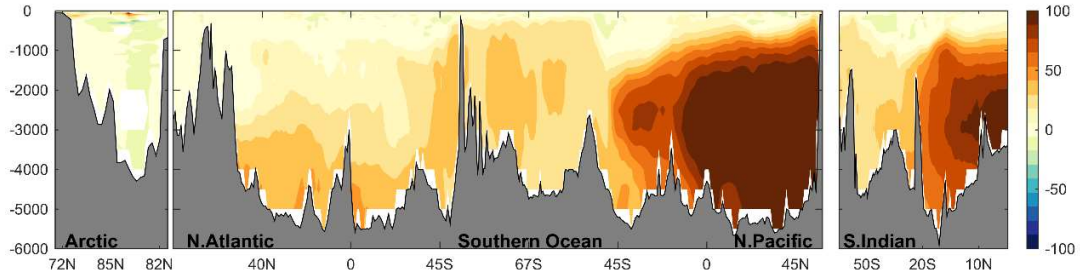

Figure S13. Crossections of TA (GLODAPv2) minus TA^0 (TMI) along the transects shown in Figure 1. The vertical axis shows depth (m) below sea level.

As a control check for the validity of our decomposition we use the estimated TA^0 (Eqn. 1) and $DIC^{PI,0}$ (Eqn. 11) to calculate preformed pre-industrial partial pressure of CO_2 ($pCO_2^{PI,0}$). We then compare this with the assumed atmospheric xCO_2 of 280 µatm in pre-industrial times (Figure S14a). It should be noted that given the calculation uncertainties (Figure S14b), which in this case represents an accumulation of all sources of error, our $pCO_2^{PI,0}$ is nowhere significantly different from 280 µatm. This lends confidence in our preformed properties, and thus in our decomposition.

On the surface our estimated $pCO_2^{PI,0}$ is on average 21±28 µatm (where the uncertainty represents one standard deviation of the mean) lower than the pre-industrial atmosphere. Though note that this is the difference compared to pre-industrial atmospheric xCO_2 and

the comparison to pCO_2 would be smaller, particularly in warm surface water. In the interior ocean areas with high AOU – like the Atlantic Ocean from surface to 1200 meter, the Pacific Ocean north of 40ºS and the Indian Ocean north of 30ºS – have $pCO_2^{PI,0}$ very close to the pre-industrial value. In other areas, particularly the polar regions, the differences are larger. In the very cold Arctic Ocean and Nordic Seas $pCO_2^{PI,0}$ is 40 to 50 µatm lower than the pre-industrial value. This is due in part to the high disequilibrium caused by a combination of strong cooling and ice cover which prevent gas equilibration, and is consistent with *Gruber et al*. [1996] which show high values of ΔC_{diseq} (-35 to -55 µmol kg^{-1}, corresponding to a pCO_2 disequilibrium of -55 to -85 µatm) in the Greenland and Norwegian Seas. The well-mixed and well-ventilated waters – like the Southern Ocean south of 45ºS – also show a highly significant disequilibrium of about -25 to -50 µatm which again is consistent with *Gruber et al.* [1996] who found a pCO_2 disequilibrium of -40 to -60 µatm at latitudes between 55ºS and 75ºS (their Figure 7). These results shown in Figure S14 are also compatible with the surface pCO_2 disequilibrium by *Pardo et al.* [2011]. They show ΔC_{diseq} of about -25 µmol kg^{-1} in the Indian sector of the Southern Ocean and -30 to 40 µmol kg^{-1} in the Pacific sector.

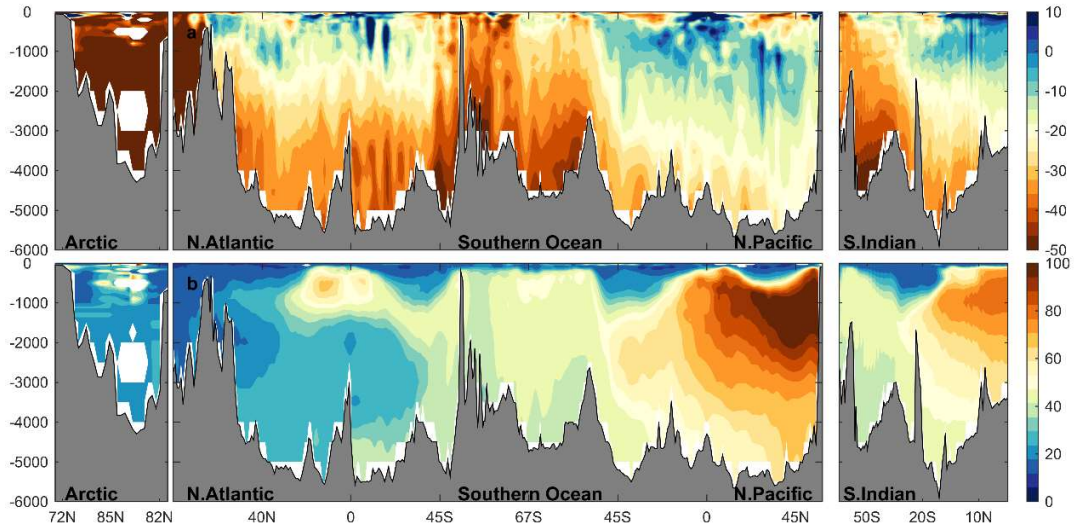

Figure S14. a) Vertical crossection of $pCO_2^{PI,0}$ (calculated from $DIC^{PI,0}$ and TA^0) minus 280 µatm. b) Uncertainty (2σ) estimate for $pCO_2^{PI,0}$. The vertical axis shows depth (m) below sea level.

Supplementary Text S6 - Natural gradients and anthropogenic change of Ω_{Ar} and Ω_{Ca}

We decomposed Ω_{Ar} and Ω_{Ca} using the same method as for pH (Eqns. 3-6). While the spatial impact of anthropogenic carbon accumulation is different on the surface (as discussed in section 4.1 in the manuscript), the effects of the natural processes are highly similar for pH (Figure 3), Ω_{Ar} (Figure S15), and Ω_{Ca} (Figure S16). While the magnitude of the different impacts vary between the variables, the relative contribution of each to the total difference between the 2002 values and the pre-industrial preformed values is the same for all variables.

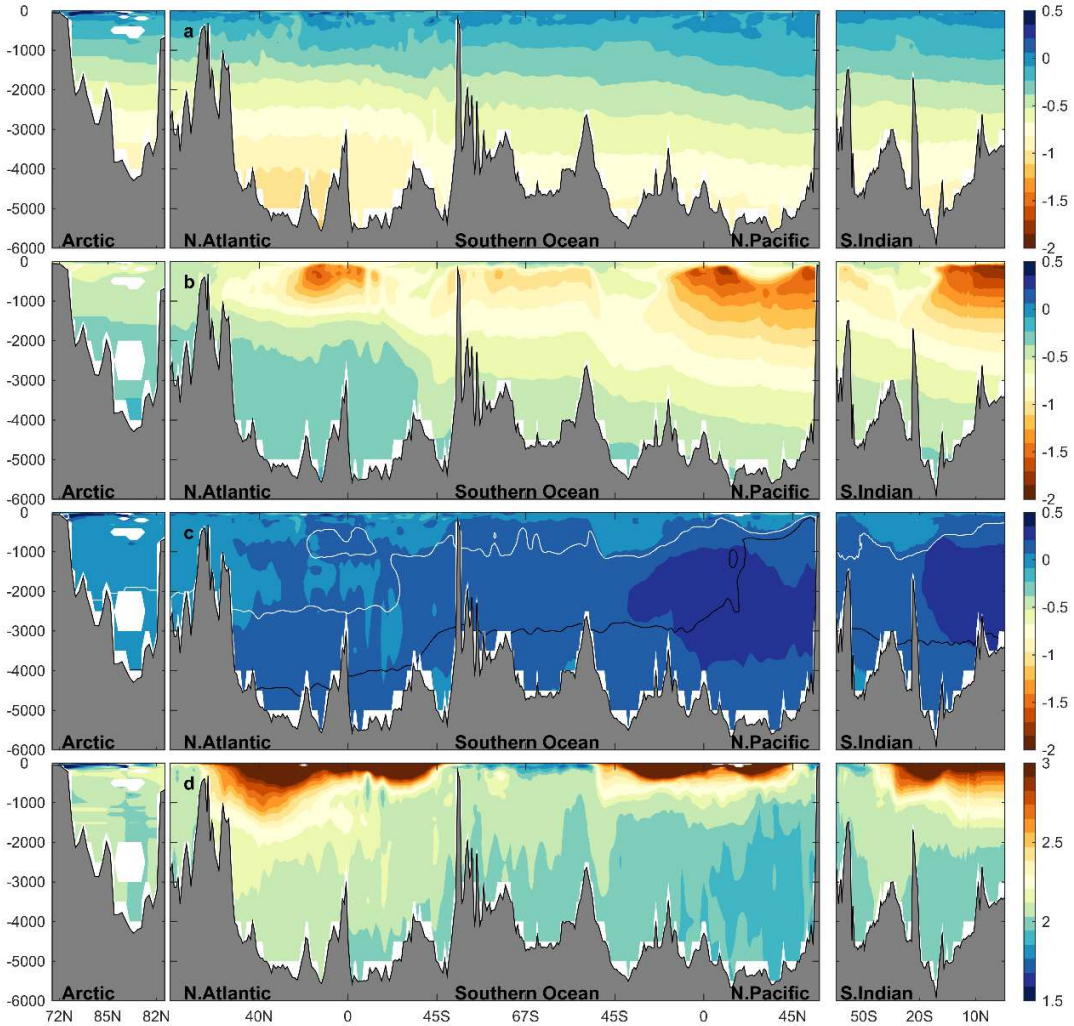

Figure S15. Same as Figure 3, but for Ω_{Ar}. The vertical axis shows depth (m) below sea level.

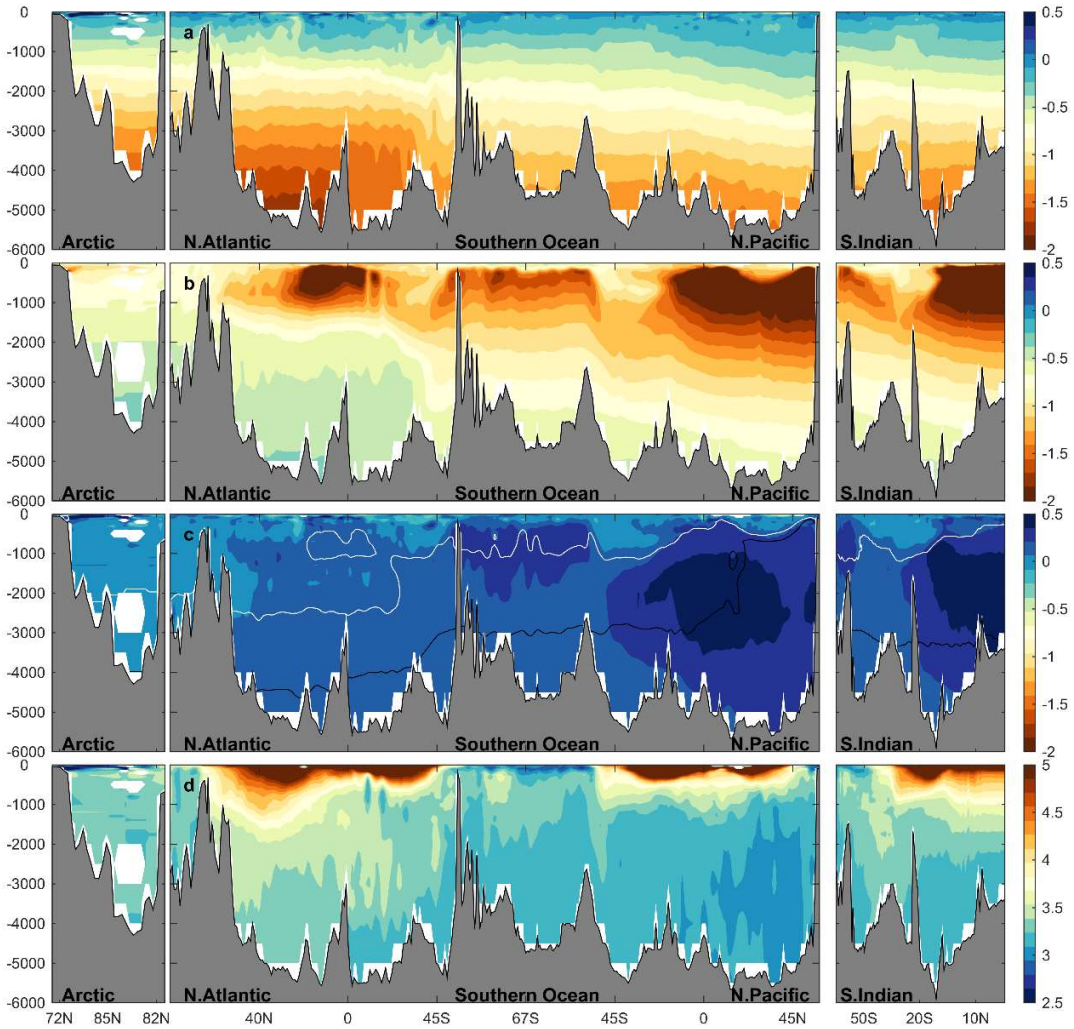

Figure S16. Same as Figure 3, but for Ω_{Ca}. The vertical axis shows depth (m) below sea level.

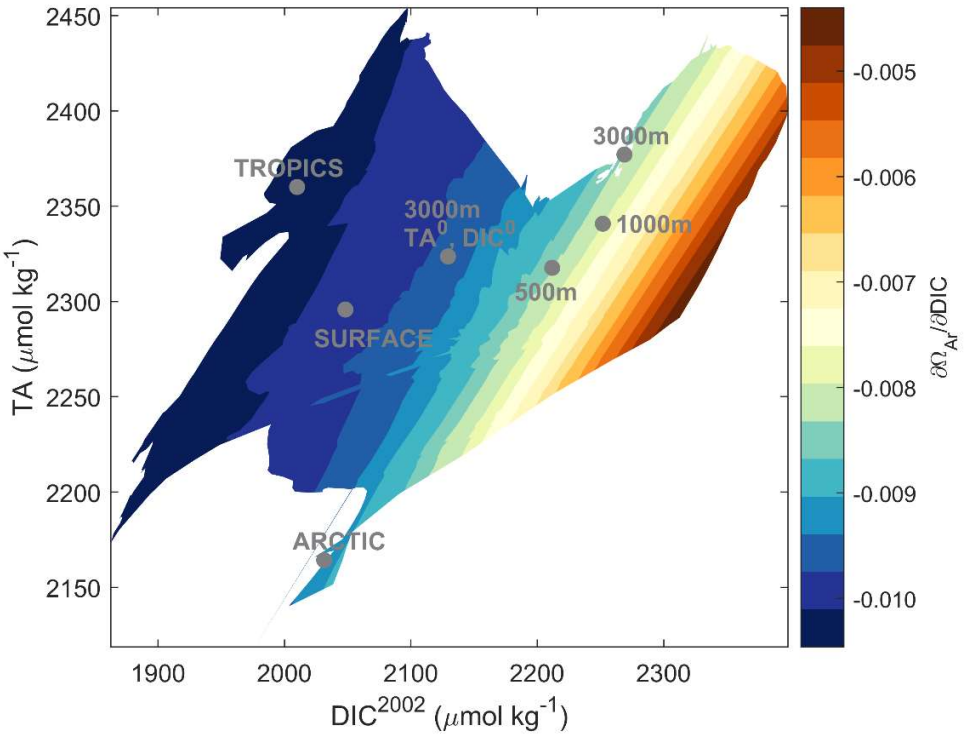

Figure S17. Visualization of the sensitivity of change in Ω_{Ar} for a given change in DIC ($\partial\Omega_{Ar}/\partial$DIC) as a function of DIC and TA. $\partial\Omega_{Ar}/\partial$DIC is calculated from the GLODAPv2 data using the derivnum function. This function is part of the CO2SYS software. Note that the sensitivity has been calculated for surface pressure (0 dbar) and 25°C in order to visualize the effects of DIC and TA only.

References

Gruber, N., J. L. Sarmiento, and T. F. Stocker (1996), An improved method for detecting anthropogenic CO2 in the oceans, *Global Biogeochemical Cycles*, *10*(4), 809-837.

Key, R. M., A. Kozyr, C. L. Sabine, K. Lee, R. Wanninkhof, J. L. Bullister, R. A. Feely, F. J. Millero, C. Mordy, and T. H. Peng (2004), A global ocean carbon climatology: Results from Global Data Analysis Project (GLODAP), *Global Biogeochemical Cycles*, *18*(4).

Lauvset, S. K., et al. (2016), A new global interior ocean mapped climatology: the 1° × 1° GLODAP version 2, *Earth Syst. Sci. Data*, *8*(2), 325-340.

Orr, J. C., J.-M. Epitalon, A. G. Dickson, and J.-P. Gattuso (2018), Routine uncertainty propagation for the marine carbon dioxide system, *Marine Chemistry*.

Pardo, P. C., M. Vázquez-Rodríguez, F. F. Pérez, and A. F. Rios (2011), CO2 air–sea disequilibrium and preformed alkalinity in the Pacific and Indian oceans calculated from subsurface layer data, *Journal of Marine Systems*, *84*(3), 67-77.